The Astrophysical Journal, 790:67 (12pp), 2014 July 20 doi:10.1088/0004-637X/790/1/67


# PRODUCTION OF FINE STRUCTURES IN TYPE III SOLAR RADIO BURSTS DUE TO TURBULENT DENSITY PROFILES

Shyeh Tjing Loi, Iver H. Cairns, and Bo Li
School of Physics, The University of Sydney, New South Wales 2006, Australia; sloi5113@uni.sydney.edu.au
*Received 2013 October 17; accepted 2014 April 19; published 2014 July 7*

## ABSTRACT

Magnetic reconnection events in the corona release energetic electron beams along open field lines, and the beams generate radio emission at multiples of the electron plasma frequency $f_p$ to produce type III solar radio bursts. Type III bursts often exhibit irregularities in the form of flux modulations with frequency and/or local temporal advances and delays, and a type IIIb burst represents the extreme case where a type III burst is fragmented into a chain of narrowband features called striae. Remote and in situ spacecraft measurements have shown that density turbulence is ubiquitous in the corona and solar wind, and often exhibits a Kolmogorov power spectrum. In this work, we numerically investigate the effects of one-dimensional macroscopic density turbulence (along the beam direction) on the behavior of type III bursts, and find that this turbulence produces stria-like fine structures in the dynamic spectra of both $f_p$ and $2f_p$ radiation. Spectral and temporal fine structures in the predicted type III emission are produced by variations in the scattering path lengths and group speeds of radio emission, and in the locations and sizes of emitting volumes. Moderate turbulence levels yield flux enhancements with much broader half-power bandwidths in $f_p$ than $2f_p$ emission, possibly explaining the often observed type IIIb–III harmonic pairs as being where intensifications in $2f_p$ radiation are not resolved observationally. Larger turbulence levels producing trough-peak regions in the plasma density profile may lead to broader, resolvable intensifications in $2f_p$ radiation, which may account for the type IIIb–IIIb pairs that are sometimes observed.

*Key words:* methods: numerical – plasmas – Sun: corona – Sun: radio radiation – turbulence

*Online-only material:* color figures

## 1. INTRODUCTION

The solar atmosphere is a highly variable environment, and activity occurs on a wide range of spatial and temporal scales. Shocks, flares, granular convection, wind shear instabilities, and other transient in situ processes in the photosphere and chromosphere generate MHD waves, which propagate upward into the corona and solar wind (Coleman Jr 1968; Jokipii & Davis Jr 1969; Tu & Marsch 1995; Horbury et al. 2005; De Pontieu et al. 2011). These are predominantly low-frequency Alfvén and fast-mode waves, which have been suggested to contribute to the heating of the corona, through a turbulent cascade that transports energy to scales small enough for dissipative processes, such as proton cyclotron damping, to convert the energy into heat (Matthaeus et al. 1999b; Cranmer & van Ballegooijen 2003; Cranmer et al. 2007). The interaction of counter-propagating Alfvén waves has been suggested as a possible mechanism for generating this turbulence (Matthaeus et al. 1999a).

Remote radio observations and in situ spacecraft measurements reveal that turbulence in the corona and solar wind exhibits a Kolmogorov power spectrum, whose inertial range spans spatial scales over many orders of magnitude (Coles & Harmon 1989; Sakurai et al. 1992; Spangler & Sakurai 1995; Spangler et al. 2002). The outer scale of the turbulence is of order 1 $R_\odot$ (where $R_\odot = 695.5$ Mm denotes the solar radius) near the surface of the Sun, and increases with radial distance from the Sun (Wohlmuth et al. 2001; Bird et al. 2002; Efimov et al. 2002). The inner scale of the turbulence, where dissipative processes become significant and the density fluctuation power spectrum steepens, is observed to occur on length scales of a few kilometers near the Sun, increasing to $\sim$100 km by about 30 $R_\odot$ (Coles & Harmon 1989; Coles et al. 1991). Although most of the turbulent energy is transported in kinetic and magnetic forms (Goldstein & Roberts 1999), fluctuations in the plasma density are expected to arise in response to fluctuations in the fluid velocity and magnetic field, and share identical spectral characteristics (Montgomery et al. 1987; Matthaeus et al. 1991; Zank & Matthaeus 1993).

Magnetic reconnection events low in the corona accelerate electrons to semi-relativistic speeds (0.1–0.6$c$), driving Langmuir waves as they travel outward along open field lines, some of which are converted into transverse radio waves at the local plasma frequency $f_p$ and/or its second harmonic $2f_p$ via the plasma emission process (e.g., Melrose 1980, 1987). These events, known as type III radio bursts, appear in dynamic spectra as rapidly drifting features, sometimes in isolation but more commonly in groups, and often exhibit harmonic structure (Wild et al. 1963; Wild & Smerd 1972; Smith 1974). In general, no type III burst is perfectly smooth: irregularities are often observed in the form of temporal shifts of parts of the envelope, or flux modulations with frequency. In extreme cases, a type III burst may appear to be fragmented into a chain of narrowband features called stria bursts, which are collectively referred to as a type IIIb burst (e.g., de la Noë 1975), where individual striae typically have bandwidths of $\Delta f/f \sim 0.1\%$–$1\%$ (Bazelyan et al. 1974a; Smith & de la Noë 1976; Bhonsle et al. 1979; Melnik et al. 2009, 2010). Type IIIb bursts (see Figure 1) are observed about as often as normal type III bursts in the decametric band, and less frequently in the metric band (Takakura & Yousef 1975; Bhonsle et al. 1979).

Many mechanisms have been proposed for the formation of type IIIb bursts (e.g., reviews by Fomichev & Chertok 1977; Bhonsle et al. 1979; Li et al. 2012). Smith & de la Noë (1976) suggested that modulational instability leads to strong beam–plasma interaction and beam–particle trapping,

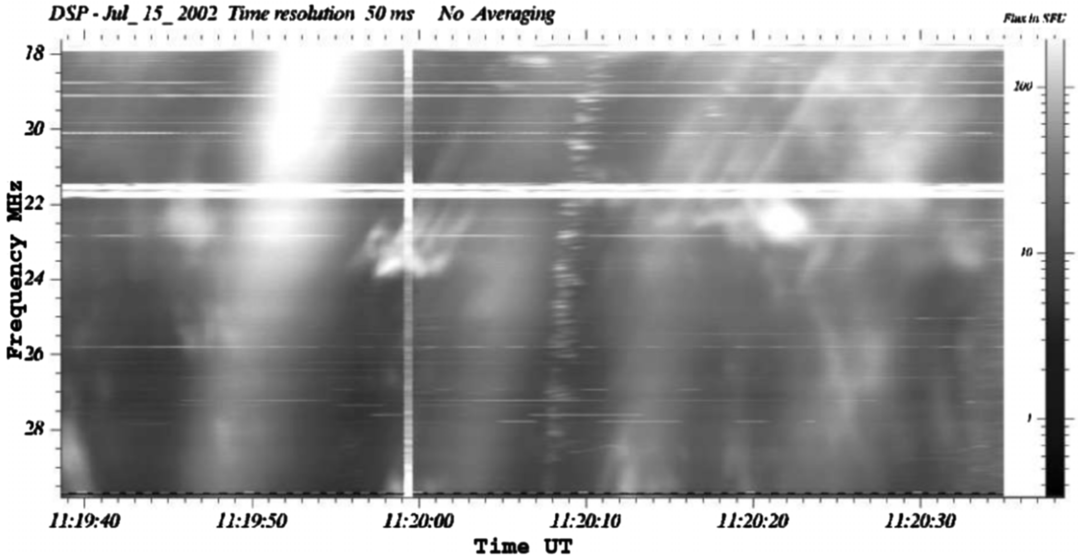


**Figure 1.** Type IIIb burst (near 11:20:10 UT) amongst type III bursts, recorded by the UTR-2 radio telescope (Melnik et al. 2010).

amplifying Langmuir waves that then decay into transverse radio waves to produce a chain of striae as the process repeats itself over the path of the electron beam. However, Cairns & Robinson (1998) argued that the predicted wavenumbers and bandwidths of Langmuir waves over a wide range of heliocentric distances are too large for modulational instability to occur directly, and therefore that this process cannot explain the fine structures in type IIIb bursts. Takakura & Yousef (1975) postulated that locally overdense and/or underdense regions in the plasma increase/decrease the interaction lengths of the beam for different frequency ranges, resulting in striae; numerical investigations (Li et al. 2012) into the proposed effects of density irregularities support this idea. There is numerical evidence that localized variations in the electron and/or ion temperatures can also give rise to stria-like fine structures (Li et al. 2011a, 2011b), and these, combined with density variations, are proposed to account for the flux modulations observed in type III bursts when their electron beams traverse coronal shocks (Lacombe & Moller Pedersen 1971; Li & Cairns 2012).

When harmonic structure is identified in a type III event, usually on the basis of a 2:1 frequency ratio and a correlation between source locations, it is often the case that the $f_p$ component of the radiation exhibits striae, while the $2f_p$ component is smooth, i.e., it occurs as a type IIIb–III pair (Ellis & McCulloch 1967; Bazelyan et al. 1974b; Takakura & Yousef 1975; Abranin et al. 1979, 1984; Melnik et al. 2011). An example of this, identified by Stewart (1975), is shown in Figure 2. Takakura & Yousef (1975) have reported as less common type IIIb–IIIb pairs, where both components possess striae, but no cases of type III–IIIb pairs. They qualitatively explained the occurrences of type IIIb–III and IIIb–IIIb pairs in terms of the differing dependences of brightness temperature on the interaction length for $f_p$ and $2f_p$ radiation, and the fraction of the source region containing density irregularities, which collectively determine whether a type III or IIIb burst is observed. Recent simulations by Li et al. (2011a) predict that localized variations in the ion temperature produce fine structures that are more pronounced in $f_p$ than $2f_p$ emission, which may also help to explain type IIIb–III pairs.

In this work, we investigate the effects of macroscopic density turbulence on the production of fine structures in coronal type III bursts, by modeling the turbulence in the source region as a power-law spectrum of macroscopic density fluctuations superposed on a smooth background density profile. We simulate the dynamics of the electron beam, Langmuir waves, ion sound waves, and electromagnetic (EM) radiation, accounting for the refraction of Langmuir waves, refraction and

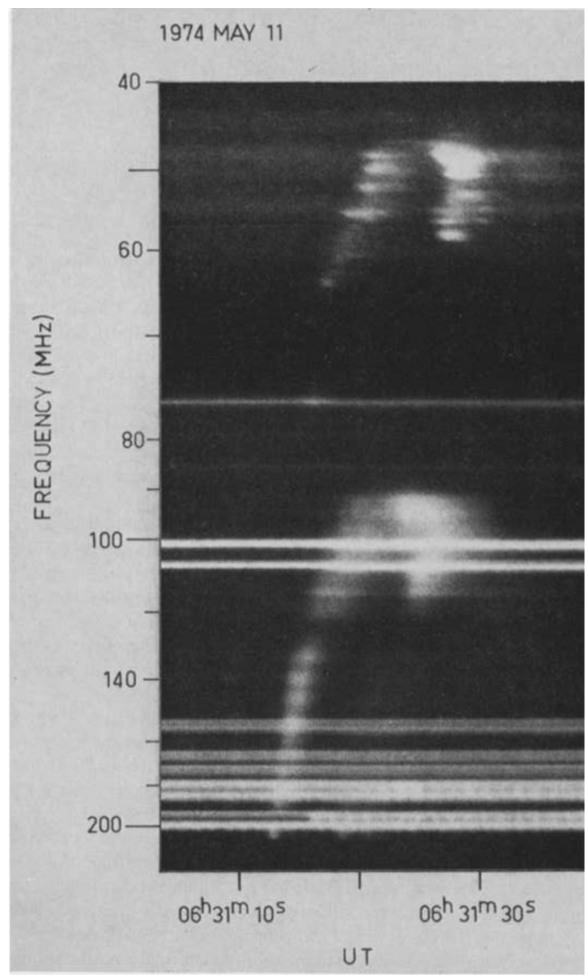


**Figure 2.** Type IIIb-III inverted-U burst recorded by the Culgoora spectrograph (Stewart 1975). The apparent striae in the harmonic component are attributed to variations in instrumental gain.

reflection of EM waves off macroscopic density variations, and the scattering of $f_p$ radiation off microscopic density fluctuations, to predict the radio emission observable at 1 AU. We find that macroscopic density turbulence alone produces flux modulations with frequency and advances/delays of the burst envelope, giving rise to stria-like fine structures in both $f_p$ and $2f_p$ dynamic spectra. We demonstrate that the emission maxima for $2f_p$ radiation originate from locally flat regions of the density profile, where source volumes are larger, whereas for $f_p$ radiation flux modulations are predominantly caused by variations in scattering losses, producing emission maxima in locally steep regions where scattering losses are lower, despite reduced source volumes in these regions. Enhancements in $f_p$ emission have bandwidths that are much broader (by a factor of $\sim 10^2$) than those of enhancements in $2f_p$ emission, which may explain observations of type IIIb–III pairs as being cases where enhancement features are only resolved in $f_p$ emission. However, when turbulence levels are large enough to produce local trough–peak regions in the density profile, the bandwidths of enhancements in the $2f_p$ emission may become resolvable. This occurs because of the presence of three disjoint regions of space spanning the same range of plasma densities, roughly tripling the flux in those frequency ranges if the structure is compact enough to fit within the spatial extent of the beam (see discussion in Section 4.1). Type IIIb–IIIb pairs may consequently result. Local temporal shifts of $2f_p$ envelopes can largely be accounted for by shifts in the locations of emitting volumes; e.g., for a beam traveling at a constant speed, a density depletion causes $2f_p$ emission at a given frequency to be produced earlier than for the smooth, unperturbed density profile. In principle this allows the turbulent density profile to be reconstructed from the time-varying frequency profile of harmonic radiation. Radiation propagation effects appear to be negligible for $2f_p$ radiation, but for $f_p$ radiation, temporal fine structures are significantly influenced by propagation effects, such as spatially varying group speeds and scattering-induced increases in path lengths.

This paper is structured as follows. In Section 2, we describe the approach to modeling density turbulence, and the simulation setup, physical processes, and assumptions incorporated into our model. Section 3 presents our results and our explanations for the production of the fine structures in $f_p$ and $2f_p$ radiation. In Section 4, we discuss the observability of the predicted fine structures in $f_p$ and $2f_p$ emission, the limitations of our work, and a numerical technique for visualizing data output onto non-monotonic grids. Finally, we conclude in Section 5.

## 2. SIMULATION SETUP

This section outlines our approach to modeling the plasma density profile in the source region, and describes the simulation setup and physical processes incorporated. Further details can be found in our previous works (Li 2007; Li et al. 2008a, 2008b, 2011a).

### 2.1. Constructing the Density Profile

We model the plasma density profile and macroscopic turbulence in one dimension (along the radial direction) as a superposition of sinusoidal fluctuations with intermediate scale lengths on a smooth background. The functional form of the coronal density profile is given by the 10-fold Baumbach–Allen model (Allen 1947)

$$n_{\rm bg}(r) = 10 n_{\rm BA} \left( \frac{2.99}{r^{16}} + \frac{1.55}{r^6} + \frac{0.036}{r^{1.5}} \right), \quad (1)$$

where $r$ is the heliocentric distance (in $R_\odot$), and $n_{\rm BA} = 10^{14}$ m$^{-3}$. This empirical model is supported by radio data (Maxwell & Thompson 1962; Stewart 1976; Benz et al. 1983). At $r = 1\,R_\odot$ (base of the corona), $n_{\rm bg} = 4.5 \times 10^{15}$ m$^{-3}$ and $f_p \approx 600$ MHz, whereas at $r = 2\,R_\odot$ (within our simulation domain), $n_{\rm bg} = 3.7 \times 10^{13}$ m$^{-3}$ and $f_p \approx 50$ MHz. The density perturbation function $\delta n(r)$ is constructed as a superposition of a finite number of sinusoids, each characterized by a wavenumber $k_i$ and modulated by a $k_i$-dependent fraction $A(k_i)$ of the unperturbed background density:

$$\delta n(r) = n_{\rm bg}(r) \sum_{i=1}^{i_{\rm max}} A(k_i) \cos(k_i r + \phi_i), \quad (2)$$

$$A(k_i) = \left( \frac{k_i}{k_{\rm min}} \right)^{\alpha/2} \Delta, \quad (3)$$

$$k_i = \frac{2\pi i}{L}. \quad (4)$$

Here $k_i$ and $\phi_i$ are the wavenumber and randomly generated phase of the $i$th mode, respectively, $L$ is the length of the source region, $\alpha$ is the index of the power spectrum, and $\Delta$ is the fractional amplitude of the mode with the lowest wavenumber, $k_{\rm min}$. The total density at any point in space is then

$$n(r) = n_{\rm bg}(r) + \delta n(r). \quad (5)$$

The form of Equation (2) implies that the power spectrum of fluctuations is

$$S(k_i, r) = n_{\rm bg}^2(r) A^2(k_i) = n_{\rm bg}^2(r) \left( \frac{k_i}{k_{\rm min}} \right)^{\alpha} \Delta^2. \quad (6)$$

Different density profiles can be generated by varying the number of modes $i_{\rm max}$, the phases $\{\phi_i\}$, the power-law index $\alpha$, and the value of $\Delta$. The simulations presented in this work use a fixed value of $\alpha = -5/3$ (the one-dimensional Kolmogorov index), $i_{\rm max}$ of either 10 or 30, and $\Delta$ either 2% or 4%. The effects of varying these parameters are discussed in Section 4.

The spatial scales of the modeled fluctuations lie within the inertial range of the turbulence observed in the corona (see Section 1). They are intermediate in the sense that they are small compared to the length of the simulation domain (280 Mm), but greater than the spatial resolution of the simulation grid (490 km) and the dissipation scales (Debye length $\lesssim 1$ m, ion inertial length $\lesssim 1$ km, ion gyroradius $\lesssim 1$ m). The simulations also include the effects of density turbulence at microscales (scales below the spatial grid resolution) as described in Section 2.2.

### 2.2. Simulation Model and Physics

The numerical model for simulating type III bursts (Li 2007; Li et al. 2008a, 2008b, 2011a) incorporates source structure, quasilinear dynamics of the electron beam and Langmuir waves, nonlinear interactions of the Langmuir ($L$), ion sound ($S$) and transverse radio ($T$) waves, and effects on the radiation propagating between the source and observer. The model considers the following emission processes (Melrose 1987; Cairns 1987; Robinson & Cairns 1993): (1) production of beam-driven $L$ waves via the bump-in-tail instability; (2) electrostatic (ES) decay $L \to L' + S$, which produces backscattered $L'$ waves and forward-going $S$ waves; (3) EM decay $L \to T(f_p) + S'$ stimulated by the products of ES decay, which produces $f_p$ radiation;

and (4) coalescence of Langmuir waves $L + L' \to T(2f_p)$, which produces $2f_p$ radiation. For EM waves, refraction due to density variations and changes in radiation group speeds within the source are incorporated. The loss mechanisms considered (Robinson & Cairns 1998) are the scattering-induced damping of $f_p$ emission via linear mode conversion (LMC) at density gradients (Kruer 1988), and free–free absorption for both $f_p$ and $2f_p$ emission; other processes are neglected.

The coronal source region is approximated by a conical frustum subtended at the Sun, between solar altitudes of $x = 630$ and 910 Mm (0.9–1.3 $R_\odot$), where $x \equiv r - R_\odot$. The source region is isothermal, with electron and ion temperatures of 1.75 MK, and has a 10-fold Baumbach–Allen density profile (Allen 1947) in the unperturbed state. We model the impulsive acceleration of electrons at time $t = 50$ ms in a small region centered at $x = 655$ Mm by replacing a fraction (0.002%) of the Maxwellian background electrons by Maxwellian electrons with a higher temperature of 15 MK. Beam development, $L$ wave growth, and the production of $S$ waves are simulated in one dimension (radially; see Kontar 2001), while $f_p$ and $2f_p$ radiation are treated in three dimensions. Radiation exiting the simulation domain is assumed to propagate in straight lines to the observer at the speed of light (differences from $c$ are negligible for our purposes), uniformly filling a cone subtended at the Sun with half-angles of 30° and 90° for $f_p$ and $2f_p$ radiation, respectively, following the assumption of isotropization by scattering off microscopic density irregularities (Riddle 1974). The dynamic spectrum $\Phi_T$ ($T = F$ for $f_p$ radiation, and $T = H$ for $2f_p$ radiation) seen by an observer positioned within the radiation cone is computed as the integral of the radio flux produced within each source layer over the length of the source region and the time span of the simulation. Details are given by Li et al. (2008a, 2008b, 2011a).

We devote the remainder of this section to expounding upon the physics of radiation scattering due to microscale turbulence (density fluctuations on length scales smaller than the spatial grid resolution), since this is central to our arguments in Section 3 for the origins of frequency and temporal fine structures in $f_p$ radiation. Unlike the macroscopic density fluctuations, which are explicitly constructed in Section 2.1, microscopic fluctuations in our model are treated statistically. They are assumed to follow a Gaussian probability distribution (Robinson & Cairns 1998; Li et al. 2008a)

$$P(\Delta n, u) = \frac{e^{-u^2}}{\Delta n\sqrt{2\pi}} \tag{7}$$

with rms level $\Delta n$ and mean length scale $\langle l \rangle$, where

$$u = \frac{n_0 - n}{\Delta n\sqrt{2}} = \frac{r - r_0}{L_0} \tag{8}$$

is the normalized position relative to a reference location $r_0$ at which the local plasma density is $n(r_0) \equiv n_0$, and $L_0$ is a characteristic length scale that depends on the local plasma density gradient. Adopting the first-order expansion about $n_0$ to obtain $n(r) \approx n_0 + n'(r_0)(r - r_0)$ implies that

$$L_0 = \frac{\Delta n\sqrt{2}}{-n'_0}, \tag{9}$$

where $n'_0 \equiv n'(r_0)$. In this work we assume a fixed value for $\Delta n/n_0 = 1\%$ (Thejappa & MacDowall 2008) and a mean length scale (after Robinson & Cairns 1998; Li et al. 2012)

$$\langle l \rangle = 2.6 \times 10^4 \left(\frac{x}{1\ \mathrm{AU}}\right)^{1.61}\ \mathrm{m}. \tag{10}$$

Since transverse waves cannot propagate below the local plasma frequency $f_p$, radiation with frequency $f$ will be scattered if it encounters a region where $f_p = f$. At these locations, the radiation becomes evanescent and is partially mode converted to Langmuir waves, which are then damped, while the rest is reflected. The scattering results in a random walk that can be modeled as a diffusion process (Robinson & Cairns 1998). This scattering effect is far more severe for $f_p$ than $2f_p$ radiation (Riddle 1974) since the former propagates very close to the plasma frequency, and so we incorporate scattering effects for $f_p$ emission only (e.g., Robinson & Cairns 1998; Li et al. 2008a). Specifically, scattering causes losses and lengthens the overall path traversed by $f_p$ emission; the latter introduces a time delay for arrival at the observer, which we model as an exponential decay.

Following Robinson & Cairns (1998) and Li et al. (2008a), the time ($t$) evolution of the probability density $p(u,t)$ of diffusing $f_p$ radiation with a frequency $f_0 = f_p(r_0)$, where $f_p(r)$ is the plasma frequency corresponding to $n(r)$, is described by the Fokker–Planck equation

$$\frac{\partial p(u,t)}{\partial t} = -\gamma(u)p(u,t) + \frac{1}{2}\frac{\partial^2 D(u)p(u,t)}{\partial u^2}. \tag{11}$$

The quantities $\gamma(u)$ and $D(u)$ are the LMC damping rate and one-dimensional diffusion coefficient (diffusivity), respectively, which are given in terms of the mean scattering length $\Delta u(u)$ and mean group speed $v_g(u)$ by (Li et al. 2008a)

$$\gamma(u) = \frac{\langle f_{\mathrm{mc}}\rangle v_g(u)}{\Delta u(u)}, \tag{12}$$

$$D(u) = \frac{1}{3}\Delta u(u) v_g(u), \tag{13}$$

$$\Delta u(u) = \frac{2\langle l \rangle}{L_0 \mathrm{erfc}(u)}, \tag{14}$$

$$v_g(u) = c\left(-\frac{n'_0 u}{L_0 n_0}\right)^{1/2}, \tag{15}$$

where $\langle f_{\mathrm{mc}}\rangle$ is the fraction of energy absorbed per reflection at a mode conversion site, averaged over incident angle and polarization. Note that the radiation can only escape when $n'_0 \leqslant 0$ and $v_g$ is real, since otherwise it is trapped and becomes evanescent. Qualitatively, one can apply a scaling argument to Equation (11), noting that $u$ is already normalized (and therefore the characteristic range in $u$ is 1), to arrive at

$$\frac{1}{\tau} \sim D, \tag{16}$$

where $\tau$ is a characteristic timescale. This relation indicates that an decreased diffusivity $D$ will lengthen the timescale of activity (for constant $\langle l \rangle$ and $n_0$), a dependence that will become relevant later in Section 3.2.

Introducing the separable solution $p(u,t) = X(u)\, e^{-\lambda t}$ turns Equation (11) into the eigenvalue problem (Li et al. 2008a)

$$\gamma(u)X(u) - \frac{1}{2}\frac{\partial^2 D(u)X(u)}{\partial u^2} = \lambda X(u), \tag{17}$$

whose solutions under absorbing boundary conditions $X(u_{\min}) = X(u_{\max}) = 0$ are characterized by a set of positive eigenvalues $\{\lambda_i\}$. We choose the boundary locations $u_{\min}$

**Table 1**
Parameters Used to Construct $\delta n(r)$ for Simulations A–C

| Simulation | $i_{\max}$ | $\Delta$ (%) |
|---|---|---|
| A | 10 | 2 |
| B | 10 | 4 |
| C | 30 | 2 |

and $u_{\max}$ such that decreasing $u_{\min}$ or increasing $u_{\max}$ produces no change in $\{\lambda_i\}$. To calculate the time constant $t_d$ for the exponential decay of $f_p$ emission at the observer, we assume $t_d$ to be determined by the smallest eigenvalue, with

$$t_d = \left(\min_i\{\lambda_i\}\right)^{-1}. \quad (18)$$

To obtain an expression for the fraction $\eta$ of $f_p$ emission, that is of frequency $f_0$ and able to escape from the source after scattering and reach the observer, we define (Li et al. 2008a)

$$\psi(u) = P(\Delta n, u)\exp\left[-\langle f_{\mathrm{mc}}\rangle \int_u^\infty \frac{du}{\Delta u}\right] \quad (19)$$

to describe the probability of emission being produced and escaping from the location $u$, which then yields

$$\eta = \frac{\int_0^\infty \psi(u)\,du}{\int_0^\infty P(\Delta n, u)\,du}. \quad (20)$$

We show in the next section that the escape fraction $\eta$ is vital in determining the frequencies of flux maxima in the dynamic spectra of $f_p$ emission.

## 3. RESULTS

Here we present the results for three simulations, denoted A, B, and C, whose plasma frequency profiles are shown in blue in Figures 3(a)–(c), respectively (see Table 1 for the parameters used to construct $\delta n(r)$ for each simulation). We discuss the simulation results by comparing them with a fourth simulation, U (for Unperturbed), whose density profile is simply the smooth background without turbulence. For simulation U the plasma frequency profile is plotted in green in Figure 3, and the $f_p$ and $2f_p$ dynamic spectra are shown in the left column of Figure 4. For simulations A–C, the predicted dynamic spectra are shown in Figures 4–6 overplotted with the envelopes of the corresponding $f_p$ or $2f_p$ burst for U (dashed contours). We will refer to advancements/delays of any burst for A–C as being with respect to these envelopes. Heating and acceleration conditions are identical for all the simulations (see Section 2.2).

To briefly summarize the results of Figures 4–6, which are analyzed in more detail in Sections 3.1 and 3.2, we find that density turbulence alone is sufficient to produce stria-like fine structures. While the $f_p$ and $2f_p$ bursts for U are smooth and featureless, the bursts for simulations A, B, and C exhibit flux intensifications/depletions with frequency and also advancements/delays of the burst envelope. We observe that the maxima in $f_p$ emission occur in locally steep regions of the density profile, due primarily to severe scattering-induced losses in locally flat regions dominating enlarged source emission volumes therein. For $2f_p$ emission, intensifications and depletions of flux with frequency are influenced mainly by

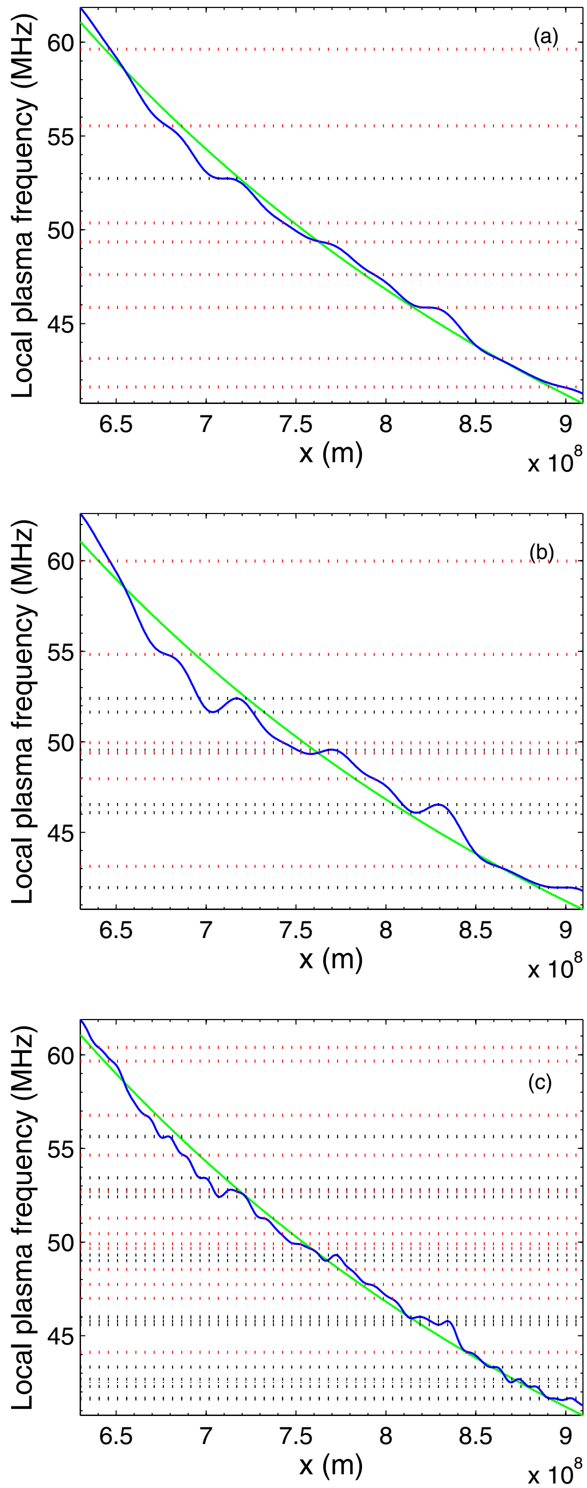


**Figure 3.** Turbulent plasma frequency profiles (blue) for simulations (a) A, (b) B, and (c) C, and the smooth 10-fold Baumbach–Allen profile for simulation U (green). Dotted red and black horizontal lines indicate inflection and stationary points in each blue profile, respectively.

(A color version of this figure is available in the online journal.)

variations in the sizes of source emission volumes, with larger source sizes leading to stronger emission, so that maxima arise in locally flat regions of the density profile. Advances and delays in the arrival of radio emission at a given frequency are due to shifts in the locations of the corresponding emitting volumes for both $f_p$ and $2f_p$ emission, but for $f_p$ emission are also due

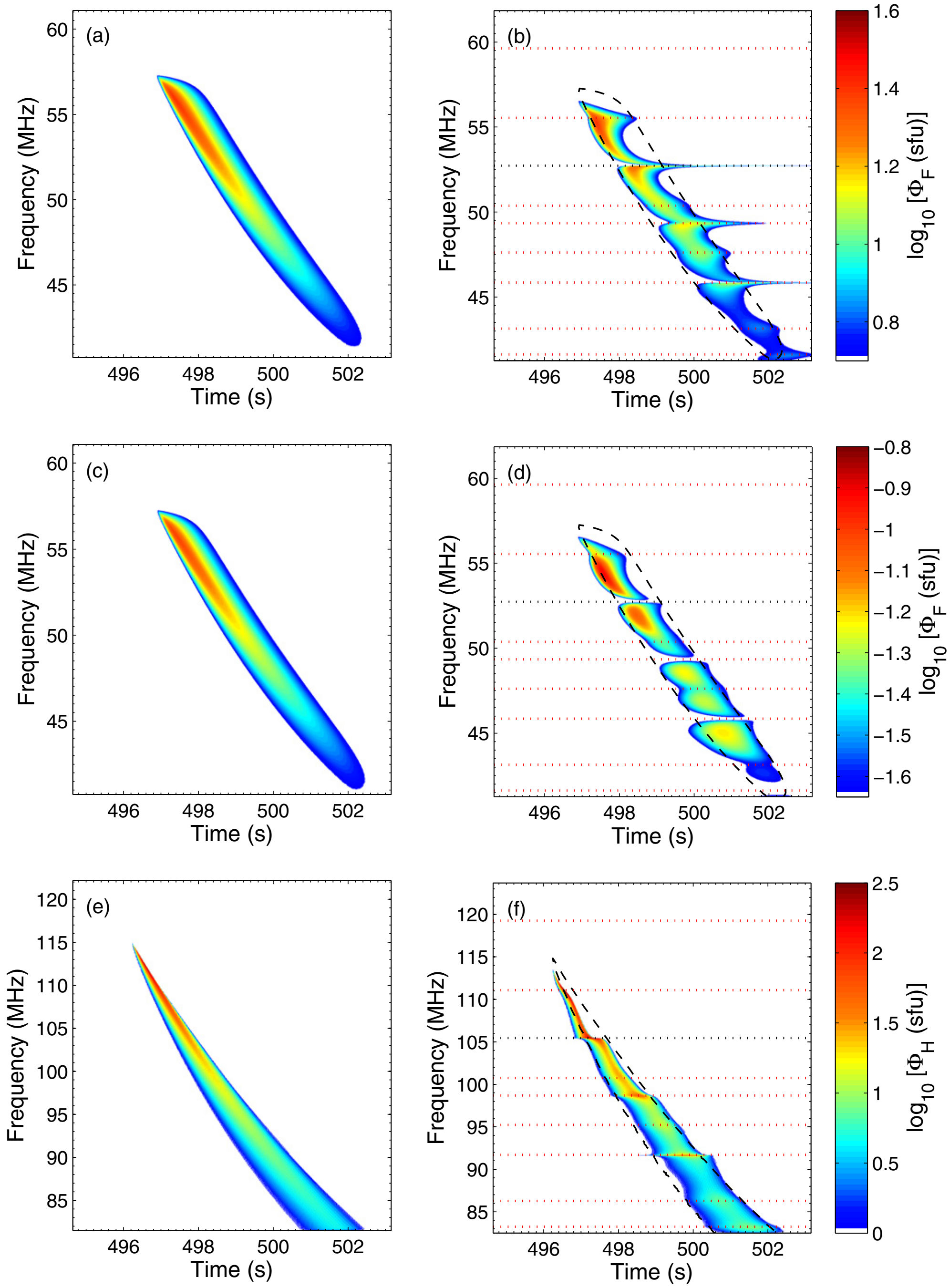

**Figure 4.** Dynamic spectra for simulations U (left) and A (right). The first two rows are $f_p$ emission, with scattering losses neglected in (a) and (b) and included in (c) and (d). The third row is $2f_p$ emission. The dashed contours on the right trace the outlines of the corresponding bursts for simulation U, and the horizontal dotted lines correspond to those in Figure 3(a).

(A color version of this figure is available in the online journal.)

to the effects of variations in the scattering mean free path and mean group speed. Our results for both $f_p$ and $2f_p$ emission show that advances and delays correspond to steep and flat regions, respectively, of the density profile, but that these advances and delays are far more pronounced for $f_p$ emission.

### 3.1. Frequency Fine Structures

Figure 4 shows the dynamic spectra of $f_p$ and $2f_p$ radiation for the smooth density profile of simulation U and the turbulent profile of simulation A, with and without scattering losses for $f_p$ emission. As expected, for the smooth background density profile the dynamic spectra (Figures 4(a), (c), and (e)) are smooth. However, flux modulations and advances/delays in the dynamic spectra (Figures 4(b), (d), and (f)) arise naturally when density turbulence is added.

When scattering-induced losses are neglected, we observe that more emission is produced at frequencies corresponding to flat regions of the density profile (i.e., $r$ values for which $n'(r) \approx 0$), since emission is produced in large volumes over small frequency ranges. Locally flat regions, defined to be where either $n'(r) = 0$, or $n''(r) = 0$ with $n'(r)n'''(r) > 0$ (this last relation is based on the realization that for a locally flat inflection point, the sign of the concavity change matches the sign of the

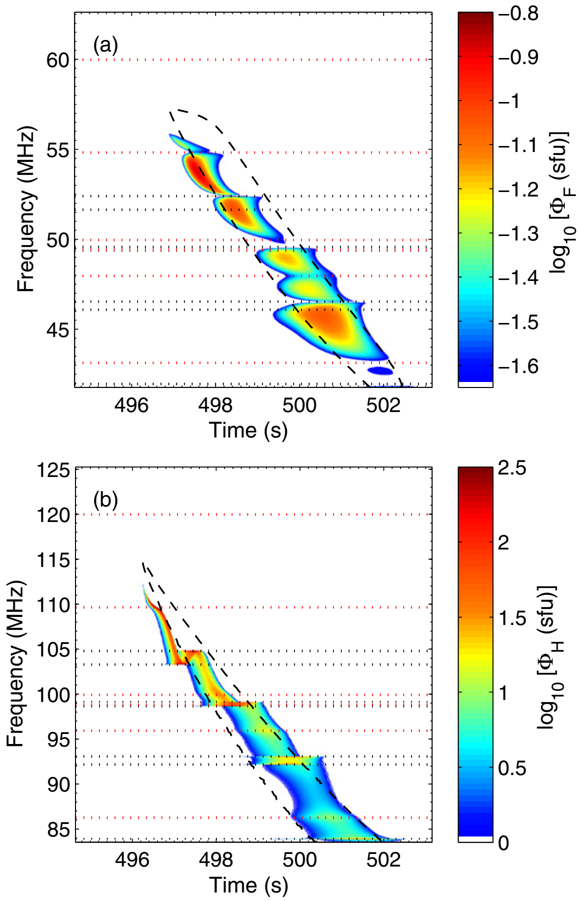


**Figure 5.** Dynamic spectra for simulation B, showing (a) $f_p$ and (b) $2f_p$ radiation. The dashed contours trace the outlines of the corresponding bursts for simulation U, and the horizontal dotted lines correspond to those in Figure 3(b).
(A color version of this figure is available in the online journal.)

gradient), and referred to below as where $n'(r) \approx 0$, are indicated by horizontal lines at corresponding frequencies in Figures 3–6. This is true of both $f_p$ and $2f_p$ emission, as can be seen from the dynamic spectra in Figures 4(b) and (f). However, once $f_p$ scattering losses are incorporated, there is a dramatic difference in the qualitative nature of the flux modulations for $f_p$ radiation: maxima now tend to occur at frequencies corresponding to steep regions of the density profile (Figures 4(d), 5(a), and 6(a)).

Physically, a photon of frequency $f$ produced near or in a region where the density profile is relatively flat ($n'(r) \approx 0$) must traverse a greater distance where $f$ is close to $f_p(r)$ than when $|n'(r)|$ is large. This increases the likelihood of the photon encountering a mode conversion region, which decreases its chances of escaping. Quantitatively, these effects can be reasoned in the context of the $f_p$ scattering model (outlined in Section 2.2) as follows. Let us define $u_c$ to be the value of $u$ at which $\psi(u)$ is maximized. To a first approximation we expect scattering to be significant for $u \lesssim u_c$, such that $\psi(u < u_c) \approx 0$, and to be negligible for $u \gtrsim u_c$, such that $\psi(u > u_c) \approx P(\Delta n, u)$ (Robinson & Cairns 1998). With these assumptions one can simplify Equation (20) to obtain

$$\eta \approx \operatorname{erfc}(u_c), \tag{21}$$

which in our simulations is observed to be within 15% of the true value given by Equation (20). Since $\langle f_{\rm mc}\rangle$ is independent of $u$, we can solve for $u_c$ using Equations (14) and (19) by setting $\psi'(u) = 0$ to obtain the following implicit relation:

$$u_c = \frac{\langle f_{\rm mc}\rangle}{4\langle l\rangle} L_0 \operatorname{erfc}(u_c). \tag{22}$$

Substituting Equation (9) into (22) then yields

$$u_c \propto \frac{\operatorname{erfc}(u_c)}{-n_0'}. \tag{23}$$

We see from Equation (23) that $u_c$ increases with decreasing $|n_0'|$, and in particular approaches infinity as $|n_0'| \to 0$. Consequently, by Equation (21), it follows that

$$\lim_{|n_0'| \to 0} \eta \approx 0, \tag{24}$$

which indicates that scattering losses are most severe for radiation having frequencies corresponding to flat regions of the density profile. This is explicitly shown in Figure 7, which reveals dramatic variations in $\eta$ (by up to two orders of magnitude) between locally steep and flat regions. As mentioned earlier, we observe that maxima in $f_p$ emission occur in locally steep regions, where $|n'(r)|$ (and therefore $\eta$) is relatively large. The effects of minimal scattering loss are partially opposed by the decrease in source volumes in these regions, since volume is inversely proportional to $|n'(r)|$, which tends to reduce the flux at frequencies where $|n'(r)|$ is relatively large. However, $|n'(r)|$ only varies by factors of 2–5 for the amplitudes of the perturbations used in our simulations, and so correspondingly, flux modulations due to variations in source volumes occur by factors of 2–5, which are very modest compared to the variations by factors of 10–100 induced by scattering effects. The latter is therefore the dominant factor in determining the locations of flux maxima/minima in $f_p$ emission.

Scattering losses are assumed to be negligible for $2f_p$ emission (Li et al. 2008a), and so in the dynamic spectra the emission maxima simply occur at regions where $n'(r) \approx 0$. This occurs because of the larger emission volume for radiation at frequencies $f \approx 2f_p(r)$ when $n'(r) \approx 0$, compared to when $|n'(r)|$ is significant.

### 3.2. Temporal Fine Structures

Assuming no other radiation propagation effects, the temporal shifts of $2f_p$ emission can be understood simply in terms of an electron beam traveling with constant speed through the corona with the given density profile. Let $f_1(x)$ be the local plasma frequency as a function of altitude $x$, and suppose that the trace of the burst in the dynamic spectrum is described by some function $f_2(t)$ representing the plasma frequency inferred (approximately half the measured $2f_p$ frequency) from the emission recorded at time $t$. Re-parameterizing $f_2$ as $\tilde{f}_2$ using

$$x(t) = v_b\, t + x_0 \tag{25}$$

so that $\tilde{f}_2(x(t)) \equiv f_2(t)$, where $v_b$ is the beam speed and $x_0 \equiv x(0)$ is some reference point. We propose that

$$\tilde{f}_2(x) \approx f_1(x). \tag{26}$$

To test the validity of Equation (26) for our simulations with turbulent density profiles, it is first necessary to derive the value of $v_b$. It has been established from previous numerical work (Li et al. 2008a, 2008b, 2009) complementing earlier interpretations

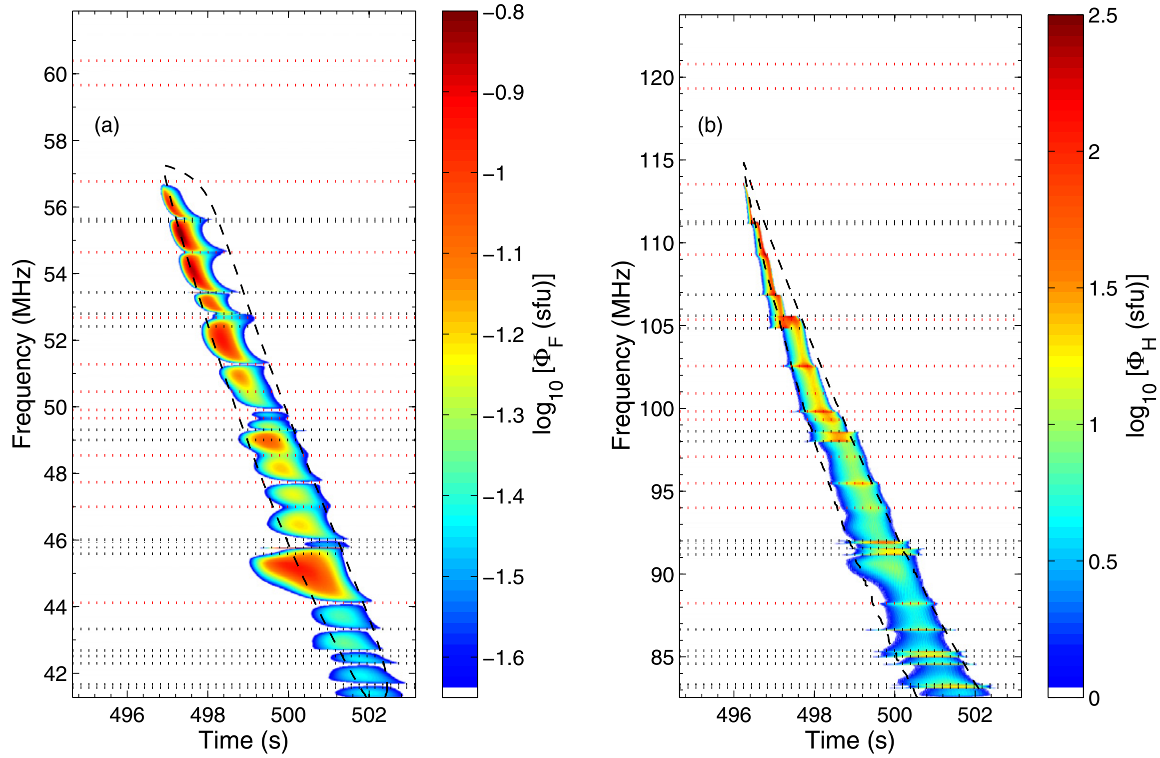


**Figure 6.** Dynamic spectra for simulation C, showing (a) $f_p$ and (b) $2f_p$ radiation. The dashed contours trace the outlines of the corresponding bursts for simulation U, and the horizontal dotted lines correspond to those in Figure 3(c).

(A color version of this figure is available in the online journal.)

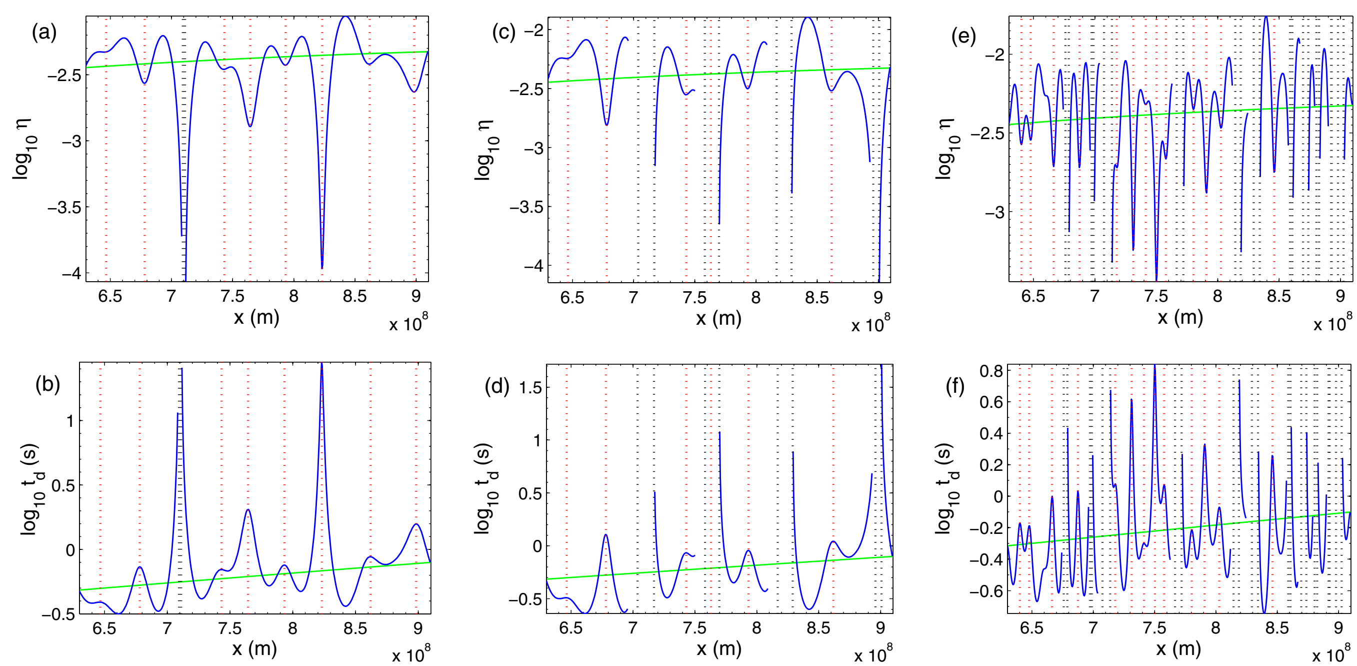


**Figure 7.** Variations in the fraction $\eta$ of escaping $f_p$ emission (top) and the time constant $t_d$ for the decay of $f_p$ emission (bottom) as a function of source position for simulations A (left), B (center), and C (right), with blue curves, and simulation U (green curves). Vertical red and black dotted lines indicate the positions of inflection and stationary points, respectively, in the corresponding density profiles in Figure 3. Gaps in the blue lines correspond to locations where $n'(r) > 0$ and the $f_p$ emission becomes evanescent.

(A color version of this figure is available in the online journal.)

of data (e.g., Wild et al. 1963), that for smooth coronal profiles the following relation holds for $2f_p$ emission:

$$\frac{df_2}{dt} = \frac{df_1(x(t))}{dt} = v_b\frac{df_1}{dx} = \frac{v_b}{2n}\frac{dn}{dr}f_1. \qquad (27)$$

In fact, Equation (27) is an equivalent statement of (26), and so we now choose to extract $v_b$ from the $2f_p$ burst of simulation U (Figure 4(e)). For each frequency value $f_2$ we obtain the time $t_{\max}(f_2)$ at which the flux $\Phi_H$ is a maximum, then calculate $dt_{\max}/df_2$ by fitting a quadratic to $t_{\max}(f_2)$ and taking the derivative of the fit with respect to $f_2$. (This is done to remove the noise associated with the raw data.) Since $f_1(x)$ is a known function, it is straightforward to compute $dx/df_1$, and so we obtain

$$v_b \approx \left\langle \frac{dx}{df_1} \left( \frac{dt_{\max}}{df_2} \right)^{-1} \right\rangle, \tag{28}$$

where $x(f_1)$ and $t_{\max}(f_2)$ are interpolated to identical $f$ values and $v_b$ is obtained by averaging the fitted beam speed for every $f$ over the whole frequency range. For the parameters used in this work we find that $v_b = 0.15c$. This value agrees with the phase-space distributions of electrons and $L$ waves in the source (not shown), which is consistent with our previous work (Li et al. 2008b, 2009, 2011a).

Using the value of $v_b$ computed from simulation U, we apply the transformation (25) to $t_{\max}$ derived from the dynamic spectra of simulations A, B, and C to obtain $\tilde{f}_2(x)$. It can be seen from the comparison between $\tilde{f}_2(x)$ and $f_1(x)$ in Figure 8 that the prediction (26) holds remarkably well for $2f_p$ emission, but not for $f_p$ emission, although we can still attribute the gross negative drift of $f_p$ emission to the overall decrease in plasma density with altitude. Since the radial falloff of the background density profile can be measured (as shown by Cairns et al. 2009 and Lobzin et al. 2010), Figure 8 demonstrates that it should be possible to directly measure the properties of intermediate-scale turbulence in the corona (and solar wind), including the levels and characteristic spatial scales as functions of heliocentric distance, using the harmonic radiation of type III bursts.

The details of temporal fine structures in $f_p$ emission appear to be influenced far more heavily by factors other than the displacement of emitting volumes associated with the density turbulence. For instance, Figure 5(a) shows an advancement of the envelope of the $f_p$ emission in simulation B in the frequency range 43–46 MHz, which is the opposite of what would be expected from the sign of the density perturbation alone: the density there is locally enhanced, and so we might expect a time delay in that frequency range. There are also tails of $f_p$ emission in A–C at frequencies corresponding to where $n'(r) \approx 0$, reflecting an increase in the characteristic timescale for the decay of $f_p$ emission produced in those locations. These can be seen clearly in Figure 4(b), for which the $f_p$ flux $\Phi_F$ at these locations is above the plotting cutoff, and in Figure 8. These fine structures result from the proportional dependence of both $\Delta u(u)$ and $v_g(u)$ on the local density gradient $n'_0$, which leads to a quadratic dependence of the diffusivity $D(u)$ on $n'_0$: from Equations (13), (14), and (15), we have

$$D(u) = \frac{2\langle l \rangle}{3\,\mathrm{erfc}(u)} \frac{c}{\Delta n \sqrt{2}} \left( \frac{u}{n_0 \Delta n \sqrt{2}} \right)^{1/2} {n'_0}^2. \tag{29}$$

Based on the dependence in Equation (16), a locally decreased value of $|n'_0|$ decreases $D$ and so lengthens the timescale $\tau$ on which $f_p$ radiation decays, whereas an increase in $|n'_0|$ gives rise to an increased $D$ and a decreased $\tau$. Figures 7(b), (d), and (f) show the variation of the time constant $t_d$ for simulations A, B, and C, respectively. It is apparent that $t_d$ peaks abruptly at positions where $n'(r) \approx 0$, and dips below the value for U where $n'(r)$ steepens locally. These quantitative results agree with our prediction. There is no dependence of the LMC damping rate $\gamma$ on $n'(r)$, and so we conclude that variations in $t_d$ are due primarily to variations in $D$ arising from the dependence of the mean scattering length $\Delta u$ and mean group speed $v_g$ on $n'(r)$.

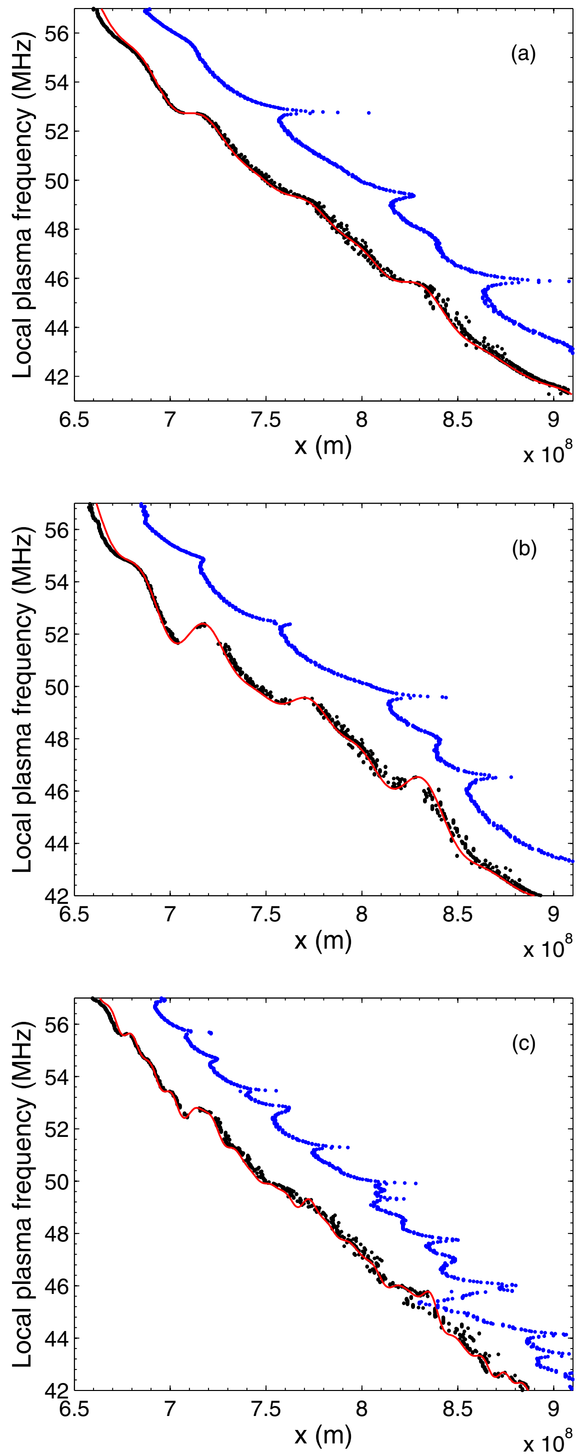


**Figure 8.** Plasma frequency profiles predicted using the $f_p$ (blue) and $2f_p$ (black) peak fluxes for simulations (a) A, (b) B, and (c) C. These predictions assume a constant beam speed of $0.15c$ and the absence of radiation propagation effects. The actual plasma frequency profiles are shown in red.

(A color version of this figure is available in the online journal.)

## 4. DISCUSSION

Although the construction of density turbulence via Equation (2) assumes radial independence of the fractional amplitude $A(k_i)$ for each mode, and the value of $\alpha$ is fixed at $-5/3$, these choices can be changed. The mechanisms suggested in Section 3 for the formation of fine structures operate wherever large-scale irregularities are present; they and the qualitative details of these structures do not depend on the detailed density profile. Therefore, our predictions are also qualitatively applicable to coronal type III bursts with different background density profiles, density turbulence with non-Kolmogorov power spectra, and interplanetary type III bursts.

The tails that appear in $f_p$ radiation at locations where $n'(r) \approx 0$ (Figure 4(b)) are not visible in the dynamic spectra when scattering losses of $f_p$ radiation are accounted for (Figure 4(d)). This is due to the severe depletions in $f_p$ flux (greatly reduced $\eta$) where $n'(r) \approx 0$, and thus in practice such tails may be difficult to detect without sufficiently sensitive instruments.

In the following subsections, we discuss the feasibility of observing the predicted fine structures in practice, limitations of our work, and resolved issues pertaining to the visualization of data written to non-monotonic grids.

### 4.1. Observational Implications of Fine Structure Bandwidths

As shown in Section 3.1, $2f_p$ emission maxima occur in the vicinity of flat regions in the density profile (e.g., at 710 and 825 Mm for simulation A). Our simulations predict half-power bandwidths $\Delta f$ for the $2f_p$ maxima that are very narrow, of order 10 kHz or less at $f \approx 100$ MHz ($\Delta f/f \sim 0.01\%$). For $f_p$ emission maxima, which occur at relatively steep sections of the density profile, the $\Delta f$ values are much larger and are determined by the spacings between locally flat regions. These spacings decrease when higher modes are added. For simulations A and B, in which the highest-frequency modes have wavelengths of 28 Mm, the $\Delta f$ values are quite large, of order 1–2 MHz for $f \approx 50$ MHz ($\Delta f/f \sim 2\%$–$4\%$), which is somewhat larger than the typically observed values of 0.1%–1% for stria bursts (Bhonsle et al. 1979; Melnik et al. 2010). Simulation C is constructed using three times the number of modes for A and B, and the highest-frequency mode has a wavelength of 9 Mm. The qualitative features present in the dynamic spectra of $f_p$ and $2f_p$ emission for A and B are also present in C, but C exhibits a larger number of irregularities due to the presence of shorter-wavelength modes. Furthermore, the bandwidths of enhancements in $f_p$ emission are smaller in C (Figure 6(a)) than A or B, ranging between 0.5–1 MHz ($\Delta f/f \sim 1\%$–$2\%$). Observations suggest (Coles & Harmon 1989; Spangler et al. 2002) that turbulence continues to occur down to length scales several orders of magnitude below that of our simulations, and so we expect the bandwidths of maxima in $f_p$ emission to be smaller in reality than those predicted by the simulations for A–C. However, the distances between locally flat regions (and therefore the values of $\Delta f$ for $f_p$ radiation) should not decrease dramatically with the addition of modes having much shorter wavelengths (larger wavenumbers), because for turbulence with a negative spectral slope, the amplitudes of these additional modes are also smaller.

The large differences in the bandwidths of $f_p$ and $2f_p$ enhancements (by a factor of $\sim 10^2$) suggest that $f_p$ enhancements should be observationally easier to resolve than $2f_p$ enhancements. Instruments that have been used to study type III bursts over the past decades have had frequency resolutions of $\Delta f/f \sim 0.05\%$–$0.4\%$ (Bhonsle et al. 1979; Stewart et al. 1981; Rosolen et al. 2001; Lobzin et al. 2009), which are insufficient to resolve $2f_p$ enhancements that are as narrow as predicted in our simulations. This may offer an explanation for the often-observed harmonic type IIIb–III pairs (Bazelyan et al. 1974b; Takakura & Yousef 1975; Abranin et al. 1984): flux enhancements are resolved in $f_p$ emission, but not in $2f_p$ emission. Among the radio instruments currently in operation, only the Murchison Widefield Array (MWA)—with its excellent frequency resolution of 10–40 kHz over the range 80–300 MHz, implying $\Delta f/f \sim 0.003\%$–$0.05\%$ (Tingay et al. 2013)—may have the capability to resolve the enhancements in $2f_p$ emission. At the time of writing, however, the full MWA has only recently come into operation, and we have yet to see its application to solar observations.

Although the bandwidths of $2f_p$ enhancements produced at regions where $n'(r) \approx 0$ may be difficult to resolve with typical instruments, broader enhancements in $2f_p$ emission may result from turbulence levels that are sufficient to produce trough-peak structures in the density profile. These broader emission features can be seen in Figure 5(b) at $f \approx 92$–93 and 98–99 MHz, where the density profile (see Figure 3(b)) is constructed from the same combination of modes as A, but with $\Delta$ twice as large. Unlike A, the density profile in B contains several non-monotonic sections. Now a trough-peak region comprises three disjoint regions of space (a downhill→uphill→downhill sequence) spanning the same range of frequency values, e.g., the 700–730 Mm and 810–840 Mm sections of the density profile for simulation B (Figure 3(b)). If the size of this region is comparable to or smaller than the radial extent of the electron beam (≈50 Mm in our simulations), then the beam at some point will encompass the whole structure, resulting in a total $2f_p$ flux $\Phi_H$ in that frequency range, that is about three times higher than $\Phi_H$ at adjacent frequencies, e.g., see the 92–93 MHz and 98–99 MHz ranges in Figure 5(b). The full-power bandwidth of an enhancement produced in this manner is equal to the difference in the local plasma frequencies of the stationary points of the structure. This difference depends on the turbulence levels and can be arbitrarily large. In such cases, both $f_p$ and $2f_p$ emission will exhibit observable flux irregularities, which may explain the observed type IIIb–IIIb events (Takakura & Yousef 1975). Note that $2f_p$ radiation is generally well above the local plasma frequency and therefore, unlike $f_p$ emission, can travel through regions where peaks exist in the density profile. This mechanism for generating flux irregularities in $2f_p$ radiation naturally rules out the possibility of type III–IIIb pairs, since turbulence levels that are sufficient to produce resolvable flux modulations in $2f_p$ emission will always produce resolvable flux modulations in $f_p$ emission as well.

### 4.2. Limitations

In this work, we have treated turbulence in the radial direction only (along the magnetic field), under the assumption that the plasma density in the source region is stratified, i.e., does not vary laterally over the width (≈240 Mm) of the simulation region. Observations and models indicate that turbulence in the corona is anisotropic, and may in fact occur to a greater extent in the plane perpendicular to the magnetic field rather than in the direction along it (Tu & Marsch 1995; Matthaeus et al. 1999a), which is at odds with this assumption. For type IIIb bursts to be formed by density turbulence, the cross sectional area of the electron beam must be small enough for density fluctuations along its path to dominate over those across its width, otherwise flux modulations might be smoothed out (see Li et al. 2012; Li & Cairns 2012). Indeed, we expect flux modulations to be less pronounced when turbulence is present in three dimensions, due to this averaging effect. Future work may therefore involve quantifying the effects of three-dimensional and possibly anisotropic turbulence on type III bursts, and assessing the likelihood of observing stria-like fine structures under these turbulence conditions.

The simulations presented in this paper that include scattering losses for $f_p$ emission predict $\Phi_F \lesssim 0.1$ sfu, which is below the sensitivity limit of typical instruments (∼1 sfu), while for $2f_p$ emission, $\Phi_H \gtrsim 2$ sfu. These results suggest that only the $2f_p$ emission will be observable. However, we assumed a Maxwellian distribution for both the thermal and accelerated electrons, whereas observations show that electron distributions in the corona have a power-law tail extending to high energies in addition to a Maxwellian component (e.g., Lin 2011). Recent work by Li & Cairns (2013) has demonstrated that the $f_p$ emission of type III bursts generated in coronal source regions with non-Maxwellian background electron populations reaches observable levels more easily than for purely Maxwellian plasmas, and also drifts faster due to greater beam speeds. Since the physical mechanisms described in Section 3 do not depend on the background electron distribution or the beam velocity, the inclusion of a high energy tail in the background electron distribution should resolve the problem of low $\Phi_F$ here without altering the qualitative features of the fine structures resulting from the density turbulence. However, this has yet to be explicitly demonstrated.

We have neglected the possible coupling of turbulence in temperature and density (e.g., via thermal pressure balance) even though it has been established that variations in electron and ion temperatures can also produce fine structures in type III bursts (Li et al. 2011a, 2011b). Our model also neglects a number of physical processes, such as the emission contribution of LMC (we have only invoked it as an absorption process for $f_p$ emission scattered by microscale density fluctuations), and the reflection and scattering of $2f_p$ radiation, which is expected to be weak but may alter the time profile of $2f_p$ flux (e.g., by introducing an exponential tail; Riddle 1974).

### *4.3. Treatment of Remote Radiation Produced in Non-monotonic Sections of the Density Profile*

One raw output of our simulations is the radio flux $\Phi_T(f, t)$ ($T = F$ or $H$) produced at each point along the spatial grid as measured at a particular time $t$ by a remote observer, where the frequency $f$ associated with each value $\Phi_T(f, t)$ is the local plasma frequency at that location. The background density profile $n_{\rm bg}(r)$ monotonically decreases with increasing $r$, but when the imposed turbulent fluctuations $\delta n(r)$ are sufficiently large, as in simulation B, local trough-peak regions in $n(r)$ are produced (e.g., Figure 3(b), between 700–720 Mm) and the vector containing the frequency values at uniformly sampled positions $x_j$ (for $j = 1, 2, \cdots, j_{\rm max}$), which we will denote $\mathbf{f} = (f(x_1), f(x_2), \cdots, f(x_{j_{\rm max}}))$, ceases to be monotonic. We identified two main complications associated with non-monotonic density profiles, namely that (1) there are occasionally duplicate $(f, t)$ pairs in the array (identical in all digits for the numerical precision used) that are associated with different $\Phi_T$; and (2) there are disjoint, contiguous sections of $\mathbf{f}$ that share no array element values in common, but span the same range of frequencies.

Problem (1) was easily dealt with by excluding all successive duplicates of $f$ in $\mathbf{f}$, which affected the resultant plots very little since this occurred at the low rate of three to four duplicate values per $j_{\rm max} = 576$ elements of $\mathbf{f}$. However, problem (2), which is a consequence of discretization, proved to be a potential source of false structure if the data were not handled carefully. The naïve approach of displaying $\Phi_T(f, t)$ on a frequency–time plot by first re-ordering $\mathbf{f}$ to obtain an ordered vector $\tilde{\mathbf{f}}$ (which is monotonic) produces jagged features in the dynamic spectra due to an interleaving of $\Phi_T$ values from disjoint regions of space when it is plotted using $\tilde{\mathbf{f}}$. For instance, $f_p$ radiation produced on the Sunward side of a density peak cannot escape to the observer and so $\Phi_F$ associated with this region is zero, but $f_p$ radiation produced over the same frequency range on the anti-Sunward side of the peak can propagate outward and thus $\Phi_F$ from this region is non-zero. If the data from these two regions are combined and plotted using $\tilde{\mathbf{f}}$, alternating zero and non-zero flux values will result, due to an interleaving of the discrete frequency values associated with the two regions.

We dealt with problem (2) by first dividing $\Phi_T(f, t)$ for fixed $t$ into piecewise-monotonic sections in frequency and interpolating each to the appropriate subrange of a uniformly spaced frequency grid, $\mathbf{f}^*$, that spans the full range of frequencies. We then formed the dynamic spectrum by arranging the individual sections onto a single frequency–time plot (with $\mathbf{f}^*$ as the frequency axis) and adding the flux values together where sections overlapped in frequency range, to arrive at a final value for the total flux at each point in time and frequency. This approach is justified by the fact that the radio flux observed remotely at a given frequency is the integral over the source region, meaning that if radiation emitted from two or more locations with the same local plasma frequency reaches the observer at the same time, the total flux measured at that frequency should be the sum of the fluxes arriving from those locations.

## 5. CONCLUSION

We have simulated the effects of one-dimensional density turbulence in the source region of a coronal type III burst and found that the turbulence produces stria-like fine structures in the dynamic spectra of both $f_p$ and $2f_p$ radiation, which otherwise are smooth when the turbulence is negligible. For $f_p$ radiation, flux modulations with frequency are governed by the effects of scattering losses, which are most severe where the density profile is flat, and so emission maxima occur in relatively steep regions of the density profile. Temporal shifts of $f_p$ radiation are caused by a combination of variations in the scattering path length and mean group speed, both of which depend on $n'(r)$, producing delayed emission where $n'(r) \approx 0$ and advancements where $|n'(r)|$ is large. For $2f_p$ radiation, flux modulations with frequency result from variations in the sizes of emitting volumes, giving rise to emission maxima where $n'(r) \approx 0$ (large emitting volume for a small frequency range), and depletions where $|n'(r)|$ is large (small emitting volume for a given frequency range). Temporal advances/delays of $2f_p$ radiation are well explained in terms of an electron beam traveling radially with a constant speed.

We demonstrated that the turbulent density profile along the beam path can be reconstructed accurately from the observed time-varying frequency of maximum flux of harmonic type III emission, since radiation propagation effects for harmonic emission are relatively minor. This result opens a new technique for probing density turbulence in the solar corona and solar wind, complementing a similar technique for the underlying smooth density profile (Cairns et al. 2009; Lobzin et al. 2010). However, due to the influence of scattering-induced time delays, a similar technique using fundamental emission does not appear viable.

Our simulations predict that the half-power bandwidths for stria-like enhancements in $2f_p$ radiation are of order $\Delta f/f \sim 0.01\%$, too narrow to be resolved by most current instruments, with the exception of perhaps the MWA, which has a frequency resolution of $\Delta f/f \sim 0.003\%$–$0.05\%$. On the other hand, the bandwidths of the enhancements in $f_p$ emission are much larger, with $\Delta f/f \sim 1\%–2\%$ for simulation C, similar to observed bandwidths of the striae. These results suggest a possible explanation for the commonly reported observations of type IIIb–III harmonic pairs (Bazelyan et al. 1974b; Takakura & Yousef 1975; Abranin et al. 1984) as being where emission enhancements are resolved in $f_p$ but not $2f_p$ radiation. When turbulence levels are large and trough–peak regions appear in the density profile having spatial extents smaller than that of the electron beam, enhancements in $2f_p$ emission with resolvable bandwidths may appear, due to the simultaneous contributions from three regions of space spanning the same range of plasma frequencies. In such cases, flux modulations with frequency are predicted for both $f_p$ and $2f_p$ radiation, and this may explain the observed type IIIb–IIIb pairs (Takakura & Yousef 1975).

Future work could involve quantifying the effects of realistic three-dimensional turbulence on the behavior of type III bursts, since the assumption of radial stratification invoked here may not be fully realistic. In addition, the effects on the flux levels of $f_p$ emission caused by a turbulent, non-Maxwellian background corona (Lin 2011) should be examined. The effects of combining temperature fluctuations and density turbulence, and the contribution of other emission processes (such as LMC), also remain to be investigated.

## REFERENCES

Abranin, E. P., Bazelyan, L. L., Goncharov, N. Yu., et al. 1979, SoPh, 62, 145
Abranin, E. P., Bazelyan, L. L., & Tsybko, Ya. G. 1984, SoPh, 91, 377
Allen, C. W. 1947, MNRAS, 107, 426
Bazelyan, L. L., Goncharov, N. Yu., Zaitsev, V. V., et al. 1974a, SoPh, 39, 213
Bazelyan, L. L., Goncharov, N. Yu., Zaitsev, V. V., et al. 1974b, SoPh, 39, 223
Benz, A. O., Barrow, C. H., Dennis, B. R., et al. 1983, SoPh, 83, 267
Bhonsle, R. V., Sawant, H. S., & Degaonkar, S. S. 1979, SSRv, 24, 259
Bird, M. K., Efimov, A. I., Andreev, V. E., et al. 2002, AdSpR, 30, 447
Cairns, I. H. 1987, JPlPh, 38, 169
Cairns, I. H., Lobzin, V. V., Warmuth, A., et al. 2009, ApJL, 706, L265
Cairns, I. H., & Robinson, P. A. 1998, ApJ, 509, 471
Coleman Jr, P. J. 1968, ApJ, 153, 371
Coles, W. A., & Harmon, J. K. 1989, ApJ, 337, 1023
Coles, W. A., Liu, W., Harmon, J. K., & Martin, C. L. 1991, JGR, 96, 1745
Cranmer, S. R., & van Ballegooijen, A. A. 2003, ApJ, 594, 573
Cranmer, S. R., van Ballegooijen, A. A., & Edgar, R. J. 2007, ApJS, 171, 520
de la Noë, J. 1975, A&A, 43, 201
De Pontieu, B., McIntosh, S. W., Carlsson, M., et al. 2011, Sci, 331, 55
Efimov, A. I., Chashei, I. V., Samoznaev, L. N., et al. 2002, ARep, 46, 579
Ellis, G. R. A., & McCulloch, P. M. 1967, AuJPh, 20, 583
Fomichev, V. V., & Chertok, I. M. 1977, R&QE, 20, 869
Goldstein, M. L., & Roberts, D. A. 1999, PhPl, 6, 4154
Horbury, T. S., Forman, M. A., & Oughton, S. 2005, PPCF, 47, B703
Jokipii, J. R., & Davis, L., Jr. 1969, ApJ, 156, 1101
Kontar, E. P. 2001, SoPh, 202, 131
Kruer, W. L. 1988, The Physics of Laser Plasma Interactions (Reading, MA: Addison-Wesley)
Lacombe, C., & Moller Pedersen, B. 1971, A&A, 15, 406
Li, B. 2007, ApJL, 666, L129
Li, B., & Cairns, I. H. 2012, ApJ, 753, 124
Li, B., & Cairns, I. H. 2013, ApJL, 763, L34
Li, B., Cairns, I. H., & Robinson, P. A. 2008a, JGR, 113, A06104
Li, B., Cairns, I. H., & Robinson, P. A. 2008b, JGR, 113, A06105
Li, B., Cairns, I. H., & Robinson, P. A. 2009, JGR, 114, A02104
Li, B., Cairns, I. H., & Robinson, P. A. 2011a, ApJ, 730, 20
Li, B., Cairns, I. H., & Robinson, P. A. 2011b, ApJ, 730, 21
Li, B., Cairns, I. H., & Robinson, P. A. 2012, SoPh, 279, 173
Lin, R. P. 2011, SSRv, 159, 421
Lobzin, V. V., Cairns, I. H., Robinson, P. A., Steward, G., & Patterson, G. 2009, SpWea, 7, S04002
Lobzin, V. V., Cairns, I. H., Robinson, P. A., et al. 2010, ApJ, 724, 1099
Matthaeus, W. H., Klein, L. W., Ghosh, S., & Brown, M. R. 1991, JGR, 96, 5421
Matthaeus, W. H., Zank, G. P., Oughton, S., Mullan, D. J., & Dmitruk, P. 1999a, ApJL, 523, L93
Matthaeus, W. H., Zank, G. P., Smith, C. W., & Oughton, S. 1999b, PhRvL, 82, 3444
Maxwell, A., & Thompson, A. R. 1962, ApJ, 135, 138
Melnik, V. N., Rucker, H. O., Konovalenko, A. A., Dorovskyy, V. V., & Tan, S. 2011, EPSC-DPS Joint Meeting 2011, Vol. 1 (Göttingen, Germany: Copernicus Group), 796
Melnik, V. N., Rucker, H. O., Konovalenko, A. A., et al. 2009, in EGU General Assembly 2009, Vol. 11 (Vienna: European Geophysical Society), 9098
Melnik, V. N., Rucker, H. O., Konovalenko, A. A., et al. 2010, in AIP Conf. Proc. 1206, Astrophysics and Cosmology after Gamow, ed. S. K. Chakrabarti, G. S. Bisnovatyi-Kogan, & A. I. Zhuk (Melville, NY: AIP), 445
Melrose, D. B. 1980, SSRv, 26, 3
Melrose, D. B. 1987, SoPh, 111, 89
Montgomery, D., Brown, M. R., & Matthaeus, W. H. 1987, JGR, 92, 282
Riddle, A. C. 1974, SoPh, 35, 153
Robinson, P. A., & Cairns, I. H. 1993, ApJ, 418, 506
Robinson, P. A., & Cairns, I. H. 1998, SoPh, 181, 363
Rosolen, C., Denis, L., Clerc, V., & Weber, R. 2001, in RFI Mitigation Workshop (Trieste, Italy: SISSA), 28
Sakurai, T., Spangler, S. R., & Armstrong, J. W. 1992, JGR, 97, 17141
Smith, D. F. 1974, SSRv, 16, 91
Smith, R. A., & de la Noë, J. 1976, ApJ, 207, 605
Spangler, S. R., Kavars, D. W., Kortenkamp, P. S., et al. 2002, A&A, 384, 654
Spangler, S. R., & Sakurai, T. 1995, ApJ, 445, 999
Stewart, R. T. 1975, SoPh, 40, 417
Stewart, R. T. 1976, SoPh, 50, 437
Stewart, R. T., Cole, T. W., Attwood, C. F., & Smith, C. J. 1981, SoPh, 71, 3
Takakura, T., & Yousef, S. 1975, SoPh, 40, 421
Thejappa, G., & MacDowall, R. J. 2008, ApJ, 676, 1338
Tingay, S. J., Goeke, R., Bowman, J. D., et al. 2013, PASA, 30, 21
Tu, C.-Y., & Marsch, E. 1995, SSRv, 73, 1
Wild, J. P., & Smerd, S. F. 1972, ARA&A, 10, 159
Wild, J. P., Smerd, S. F., & Weiss, A. A. 1963, ARA&A, 1, 291
Wohlmuth, R., Plettemeier, D., Edenhofer, P., et al. 2001, SSRv, 97, 9
Zank, G. P., & Matthaeus, W. H. 1993, PhRvA, 5, 257